Journal Name

ARTICLE TYPE

Cite this: DOI: 00.0000/xxxxxxxxxx

Slow surface diffusion on Cu substrates in Li metal batteries†

Ingeborg Treu Røe[a] and Sondre Kvalvåg Schnell[a]

Received Date
Accepted Date

DOI: 00.0000/xxxxxxxxxx

Dendrite growth on the lithium metal anode still obstructs a widespread commercialization of high energy density lithium metal batteries. In this work, we investigate how the crystal structure of the copper foil current collector influences the morphology of the lithium anode and the mobility of lithium on the anode using density functional theory and molecular dynamics simulations. We have developed an adaptive Common Neighbour Analysis, *surface adaptive Common Neighbour Analysis*, that provide insights into the surface crystal structure of the lithium anode and its impact on the *surface diffusion barrier* of lithium. The surface diffusion barrier is in turn used as an descriptor for dendrite formation. Our analyses reveal that the mobility of lithium on the anode is drastically enhanced when the lithium anode inherits the close-packed fcc crystal structure of the copper foil current collector; the surface diffusion barrier is reduced by more than six times compared to a copper-free lithium anode. However, the large lattice mismatch between lithium and copper creates vacancies and disorder in the lithium anode, which reduce the mobility of lithium. The results provide an atomistic explanation for the lithium dendrite growth observed on copper current collectors as well as a guideline to find alternate anode current collectors that can reduce the formation of dendrites.

1 Introduction

Enhancements in the energy density of the lithium ion batteries (LIBs) are called for to help the transition from fossil fuels to renewable energy sources[1]. Utilizing the Li metal anode can improve the specific energy density by 50% on the cell level[2]. However, moss-, needle- or bush-like structures called dendrites forming on the metal anode upon charge and discharge deteriorate the anode, and ultimately short-circuit the battery. The dendrite formation is not fully understood, but the applied voltage and current density[3–7], as well as the chemical and mechanical environment[8–12], affects the dendrite formation. This understanding has lead to techniques to reduce dendrite growth, including surface engineering and nanostructuring of the anode[13–17], electrolyte additives[18–20] and solid state electrolytes[21], and manipulation of the solid electrolyte interphase (SEI)[20,22–24]. Due to the complexity of the battery, it is difficult to separate different nucleation and growth mechanisms from one another, and neither the composition of the electrolyte nor the current density can completely explain why Li is more susceptible to dendrite formation than other metal anodes[25]. In particular, the Mg metal anode is less susceptible to dendrite formation[26].

It is suggested that *surface diffusion barriers* (SDBs) of adatoms on a metal surface, can serve as descriptors for dendrite growth[27]; the higher SDB associated with more sluggish surface diffusion on the metal surface, is thought to enhance uneven deposition, while a lower SDB increases the distribution of adatoms on the surface and reduces the dendrite formation. This suggestion is based on density functional theory (DFT) calculations, finding the SDB of Li to be higher than that of Mg[27], and is supported by kinetic Monte Carlo models indicating that the SDB affects the morphology of metal deposits[28]. While a direct relation between the SDB and experimentally observable quantities is challenging to establish[29], and no studies to our knowledge verify the use of the SDB as a descriptor for dendrite formation, the mobility and rearrangement of adatoms on the surface, and the subsequent surface and substrate structure are important for the formation of dendrites on Li surface[25,30]. This supports the assumption that the SDB can describe the dendrite formation. On the other hand, an applied electric field can increase the SDB of adatoms on Mg surfaces above that of Li surfaces[31], conflicting the use of SDB as the sole descriptor for dendrite formation on a metal surface. Nonetheless, the SDB can give valuable information on the behaviour of metal surfaces, and contribute to the understanding of how and why dendrite formation arises.

In a previous study, we found that the differences in crystal structure between Li and Mg can contribute to the differences in the SDBs found by Jäckle and co-workers[27]. We suggested that,

[a] *Department of Materials Science and Engineering, Norwegian University of Science and Technology, Trondheim, NTNU, Norway. E-mail: sondre.k.schnell@ntnu.no*

† Electronic Supplementary Information (ESI) available]. See DOI: 00.0000/00000000.

on a general basis, more close-packed structures exhibit lower SDBs[32], explaining why Mg which crystallizes in the hcp structure at room-temperature exhibits lower SDB than Li, whose room temperature crystal structure is bcc. It is worth noting that the electronic configuration of Li and Mg contributes to the respective SDBs. Whether the SDB of a close-packed structure is lower than that of the less dense structures might therefore depend on the metal in question.

The surfaces modelled in this previous study were flat metal surfaces without substrates present, but in commercial LIBs the anode is supported by a current collector, typically a Cu foil[33]. Cu anode current collector is the favoured choice owing to its excellent electronic and thermal conductivity and electrochemical stability in the voltage window of the Li anode[33,34]. Although atomistic studies on the interaction between Cu and Li has found that Li can diffuse through a Cu thin-film[35], the diffusion barrier is for monovacancy assisted Li diffusion is 670 meV, implying that the Cu current collector is relatively stable toward Li and that Cu-Li alloying occurs to a small extent. Furthermore, the binding energy between the Li adsorbed on a Cu current collector is found to be sufficiently high to facilitate more even and smooth deposition of Li than on a C-based surface such as graphite[36], but Cu foils are still associated with dendrite formation[37]. Manipulation of the current collector surface reduces these issues by providing higher surface area and lower current densities, accommodating the volume change of the anode during cycling, and relieving the Li metal anode of stress formed during electrodeposition[15,38–40]. The manipulation techniques highlight the importance of the current collector morphology and structure, but how these factors impact the Li dendrite formation on an atomic level remain unknown. A better understanding of the atomistic mechanisms underlying the current collector-Li surface interaction and its impact on the dendrite formation, can aid the design of future current collectors that reduce Li's tendency to form dendrites.

In the present work, we use the SDB as an indication of the propensity of a surface to form dendrites, and investigate the impact of the Cu current collector on the Li surface diffusion using DFT. Additionally, we study the influence of the Cu substrate on the surface crystal structure of Li using molecular dynamics (MD) simulation in combination with the *surface adaptive Common Neighbour Analysis* (sa-CNA) modified herein for binary surfaces. Our results show that Li on the Cu foil current collector is prone to form dendrites due to the vacancies created in the deposited Li surface as a response to the lattice mismatch between Li and Cu. The vacancies increase the Li adatom SDB through two mechanisms; firstly, the density of the deposited Li surface decreases. Secondly, they increase the impact of the poor local electronic overlap between the p- and d-orbitals of the surface Cu atoms and the s- and p-orbitals of the Li adatom. These two mechanisms result in a Li surface that might be prone to dendrite formation even if the Cu foil current collector could facilitate deposition of Li in close-packed crystal structures which can decrease this tendency.

Simulation Details

DFT Simulations

The SDBs were calculated using the DFT code Vienna *Ab intio* Simulation Package (VASP)[41,42] together with the climbing image Nudged Elastic Band (c-NEB) method[43–46]. The Li_sv and Cu_pv projector augmented wave pseudopotentials[47] were expanded to energy cutoffs of 500 eV for the pure Li simulation cells, and 550 eV for the pure Cu as well as the combined Cu-Li simulation cells. The PBEsol functional[48] was used. The c-NEB calculations were performed on simulation cells exposing the (001) and (111) fcc facet with periodic boundary conditions and dimensions exceeding 14 Å in all directions, plus a vacuum of more than 15 Å in the z-direction. The stability of the surface in the Cu simulation cell was tested in Fig. S1† as a function of the z-dimension (without vacuum). The four uppermost layers of atoms in the z-direction were free, while the rest of the atoms were fixed in space to mimic the bulk. All bulk and surface cells were relaxed to within 0.001 eV/Å. c-NEB was performed on five images for each surface diffusion path, and the maximum force on each of the images was relaxed to within 0.01 eV/Å.

Molecular Dynamics Simulations

Molecular dynamics (MD) simulations were performed using the Large-scale Atomic/Molecular Massively Parallel Simulator (LAMMPS)[49] with MEAM-potentials[50] for Li and Cu. The melting points of Li and Cu were investigated to evaluate the accuracy of the potentials. The calculations were performed using the isobaric-isothermal ensemble (NPT) with a Nose-Hoover thermostat and barostat[51] on simulations cells containing 500 particles and periodic boundary conditions. The pressure was kept constant at 1 bar for all simulations. Further information on the scheme used for the melting point simulations is found in the ESI†. The melting points of Cu and Li were found at around 1330 °C and 110 °C, which is 250 °C higher and 70 °C lower than the experimental melting points[52], respectively. This implies that the Cu-Cu interaction is slightly stronger and the Li-Li interaction slightly weaker than experimentally observed. However, the NPT scheme used here is associated with relatively high uncertainties[53]. Here, we model systems away from the melting point of Li and Cu. Additionally, we find that the 0 K lattice constants of Cu and Li at 3.62 Å and 3.51 Å (calculated as described in the ESI†) correspond well with DFT calculated values at 3.62 Å[54] and 3.44 Å[27]. They are also in agreement with the experimental values at 3.60 Å[55] and 3.51 Å[56] for Cu and Li, respectively.

The MD simulations of the Li and Cu-Li cells were performed in the canonical (NVT) ensemble with the Nose-Hoover thermostat for temperatures of 10 K, 50 K, 150K, 200 K, 250 K and 300 K on Cu-Li and Li simulation cells containing 4000 and 4400 particles, respectively. The Cu-Li simulation cells consist of 3800 Cu bulk and 200 Li surface particles initialised in the fcc (001) structure. Periodic boundary conditions were used in all directions, and an initial vacuum exceeding 140 Å was added in the z-direction (normal to the surface) for both the Cu-Li and Li simulation cells. The simulation cells were relaxed using the damped dynamics minimization method[57], equilibrated for 0.01 ns with 0.01 ps thermo-

stat relaxing time, and then ran for 1 ns with 0.1 ps thermostat relaxing time. Position data was sampled every 0.1 ps and 1 ps for the equilibration and run. An *adaptive Common Neighbour Analysis* (a-CNA) method for binary surfaces with AA-termination developed in this work, was used to analyse the position data from the MD simulations. This modified a-CNA method, the *surface adaptive Common Neighbour Analysis* (sa-CNA), is based on the a-CNA routine for single-element bulk cells as implemented in Ovito[58,59]. Information on and testing of the sa-CNA routine are described in the ESI†.

Results and Discussion

Li Surface Diffusion on Cu Substrates

Previously, we showed that higher degree of close-packing reduces the SDB of adatoms on the surface[32]. We find a similar trend for the SDB of adatoms on a Li surface with and without a Cu substrate in Fig. 1(a) and (b). Here, the Cu inhabits it's room temperature bulk structure, fcc, while the Li surface (in Fig. 1(b)) is created as described in the ESI†, where all of the Cu fcc (001) hollow positions are inhabited by a Li atom. Consequently, the surface density is 31.1% higher than that of the Li surface without a substrate due to the lattice mismatch between Cu and Li. This decreases the SDB of the adatom by more than 600%. Thus, the Cu substrate facilitates the growth of an ultra close-packed Li surface with low SDB, which can reduce the Li dendrite growth.

However, it is unlikely that the Li surface remains in such an extremely close-packed state. Table 1 suggests that vacancies are formed, as the energy per surface atom decreases with increasing amount of vacancies for the fcc (001) surface. Here, the energy is given by:

$$E_{surf}^{atom} = \frac{E_{surf} - E_{bulk}}{N_{surf}} \quad (1)$$

where E_{surf} is the energy of the relaxed simulation cell with the surface layer, E_{bulk} is the energy of the relaxed simulation cell without the surface layer (*i.e.* with one layer less in the normal direction) and N_{surf} is the number of surface atoms. The ratio of vacancies is given by the number of vacancies, N_{vac}, over the total number of surface atoms, $N_{tot,surface}$, as $\frac{N_{vac}}{N_{tot,surface}}$. The last entry in Tab. 1 refers to a surface where the lattice mismatch between the Cu bulk and the Li surface is less than 3%, making a realistic epitaxial growth case[60].

Table 1 Energy per surface atom ($eV/atom$) for fcc (001) Li surface with varying ratio of vacancies, where the ratio is given by the number of vacancies over the total number of surface atoms. The last entry refers to a surface with a lattice mismatch of less than 3%.

Ratio of vacancies (%)	Energy ($eV/atom$)
0	-2.375
3.13	-2.392
6.25	-2.409
43.75	-2.491

When vacancies are introduced, the interaction between Li and Cu become more important. Therefore we investigated the surface diffusion of Li on a clean Cu substrate. The SDB of the Li adatom on this surface is shown in Fig. 1(c). Compared to Fig. 1(a), the SDB is almost 10 times higher even though the Cu surface is more closely packed relative to the Li adatom than the Li surface. This suggests that inherent properties of Cu affect the mobility of Li.

The local electronic structure of and around the Li adatom can affect the SDB[32], and can contribute to the different SDB of the Li and Cu substrate observed in Fig. 1(a) and (b). Using DFT we therefore investigated the local electron density of and around the Li adatom. Figure 2(a) and (b) depict the overlap in the partial density of states (p-DOS) between the Li adatom and the uppermost surface layer for a Cu and Li surface, respectively. The p-DOS describes the probability of an energy level to be occupied by electrons, and Fig. 2(a) and (b) show the occupied energy levels shared by the adatom and the surface. Small spacial overlaps between the adatom and the surface mean that the local electronic mobility is poor, which is the case for the Li adatom on the Cu substrate. The Li surface, on the other hand, exhibits better spacial overlap between the adatom and the surface as shown in Fig. 2(b), implying better local electronic mobility on the Li surface. Figure 2(c) and (d) show the total density of states (DOS) resolved on the s-, p- and d-orbitals for the adatom and the surface atoms in the uppermost layer separately. In Fig. 2(c) the total DOS of the adatom overlaps poorly with the total DOS of the Cu surface. The poor overlap in energy arises from an incompatibility of the Cu surface 3d-orbitals and the Li adatom 2s-orbitals, explaining the small overlap in p-DOS in Fig. 2(a). Thus, the ability to rearrange the electrons shared by the Cu surface and the Li adatom might decrease, which increases the SDB. In contrast, the 2s- and 2p-orbitals of the Li adatom naturally overlap well with orbitals of the Li surface (Fig. 2(e)), and enable a fast reorganization of the electrons upon surface diffusion of the adatom, which can reduce the SDB. In other words, the local electronic structure of and around the adatom contributes to the mobility of the adatom. The mobility can decrease significantly when the orbitals of the adatom and the surface are incompatible, as is the case for the Li adatom on a Cu substrate.

Notice that the electrode potential is disregarded in the DOS calculations. An applied potential will pull the Fermi level of the Cu orbitals upwards, and increase the energy overlap between the total DOS of the Li adatom and Cu surface, which can decrease the SDB. Hence, an appropriate electrode potential might be important to include in the SDB and DOS calculations to accurately describe the behaviour of the Li adatom on the Cu substrate during battery operation. On the other hand, screening of the electric field by the metal substrate can reduce the impact of the electric field on the adatom SDB[61]. Consequently, the SDB of the Li adatom on a Cu substrate might be higher than that of Li on a Li substrate due to local poor overlap between the DOS of the Li adatom and the Cu substrate even when the electrode potential is considered.

Although Fig. 1(b) showed that epitaxial growth of a Li surface on the Cu substrate creates an ultra-dense fcc surface with low SDB, the Cu-Li lattice mismatch is too high for the surface to stay in the close-packed state. Consequently, vacancies are introduced in the surface, and the density of the overlaying Li surface is reduced. This can increase the adatom SDB due to the poor electronic overlap between the Cu substrate and Li adatom or-

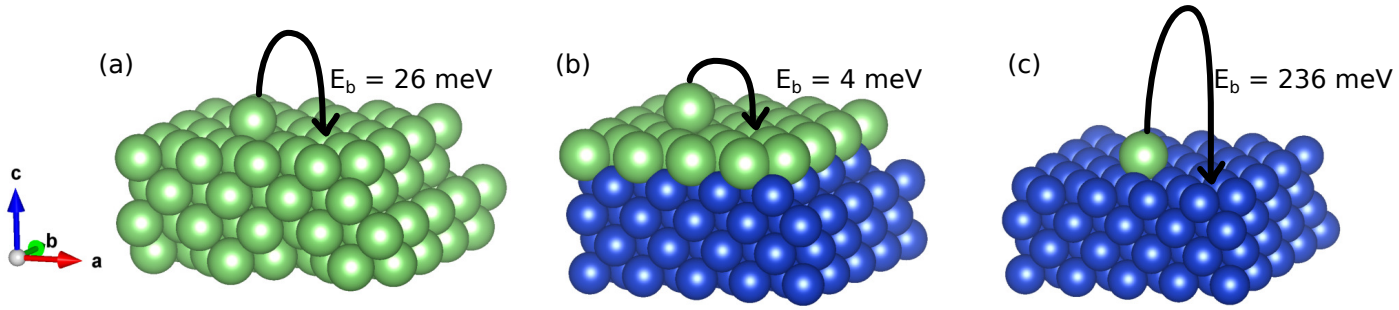

Fig. 1 The SDB of Li on different fcc (001) substrates; (a) flat Li substrate, (b) Cu substrate with a flat Li surface, and (c) flat Cu substrate.

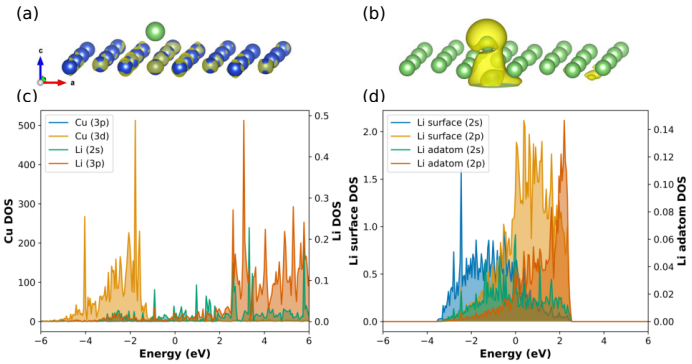

Fig. 2 The spacial extension of the p-DOS of Li on different fcc (001) substrates; (a) flat Cu substrate and (b) flat Li substrate. The DOS of resolved on the first surface layer and the Li adatom for (c) Li adatom on Cu substrate (from (a)), and (d) Li adatom on Li substrate (from (b)).

bitals.

Li Vacancy Surface Diffusion

The Li vacancies are important for the mobility of the Li adatoms on the Cu substrate, but to fully understand their impact on the surface mobility, we have investigated the SDB of single vacancies in surfaces with different crystal structures. Table 2 shows the single vacancy SDB in surfaces with different crystal structures compared to the adatom SDB on a clean surface with the corresponding crystal structure. Although the SDBs are relatively low, particularly for the fcc surfaces, the vacancies generally have higher SDBs than the adatoms. Hence, the major mechanism of transport in and on the Li surface is adatom surface diffusion.

Additionally, the vacancy SDB can affect the accumulation of vacancies in the surface; Higher vacancy SDBs can lead to single vacancy accumulation in the surface[62]. Since the single vacancy SDBs of the bcc are higher than those of the fcc surfaces, the bcc surfaces might be more prone to single vacancy accumulation. Whether the difference in single vacancy diffusion of the bcc compared to the fcc surfaces is unique for Li or if it is an effect of the crystal structure, is unclear. Furthermore, the magnitudes of the bcc single vacancy SDBs might still be too low for the vacancy accumulation to be a prominent mechanism[62].

Table 2 Energy barriers of vacancy and adatom surface diffusion for Li bcc and fcc structures

		Li	
		Adatom (meV)	Vacancy (meV)
bcc	001	53	181
	110	38	12
	111	139	289
fcc	001	25	25
	110	22	35
	111	36	73

Surface Crystal Structure

We now return to the electrodes where a layer of Li is deposited on a Cu surface. As discussed, the adatom SDB is affected by the surface crystal structure, as well as the amount of vacancies in the surface; a more close-packed surface reduces the SDB compared to the less dense and vacant surfaces. At temperatures close to 0 K, Li is table in the fcc crystal structure, but it experiences a phase transition to the bcc structure at increasing temperatures[63]. The Cu substrate is stable in the fcc bulk structure both at 0 K and room temperature, and could facilitate epitaxial growth of the first deposited Li layers. However, the DFT calculations show that the lattice mismatch between Cu and Li introduces vacancies in the Li surface, which can distort the surface crystal structure. To investigate further the impact of Cu on the crystal structure of the Li surface, MD simulations in combination with the sa-CNA of Cu-Li simulation cells were performed. Figure 3 shows the surface crystal structure of the Li surface on a Cu substrate at 300 K as a function of time. The weighted number of particles is the ratio of atoms in a crystal structure over the total number of surface atoms. The labels fcc(001), fcc(111) and fcc(001)fcc(111) denote a fcc(001) surface and substrate (*i.e.* the crystal structure of both the surface and the uppermost substrate layer is fcc(001)), a fcc(111) surface and substrate, and a fcc(001) substrate with a fcc(111) surface.

This Cu-Li simulation cell was initialized with the 0 K Cu lattice constant and Li atoms occupying all Cu fcc (001) hollow sites, meaning that the initial lattice mismatch is 17%. The surface atoms retain their initial fcc(001) structure through the first 0.01 ns at 300 K in Fig. 3. Subsequently, the unrecognized structure (other) replaces the fcc structure (fcc(001), fcc(111) and fcc(001)fcc(111)). As the surface approaches equilibrium at 0.6 ns, the ratio of fcc(001)fcc(111) surface atoms increases, but never exceeds the amount of unrecognized atoms. The immedi-

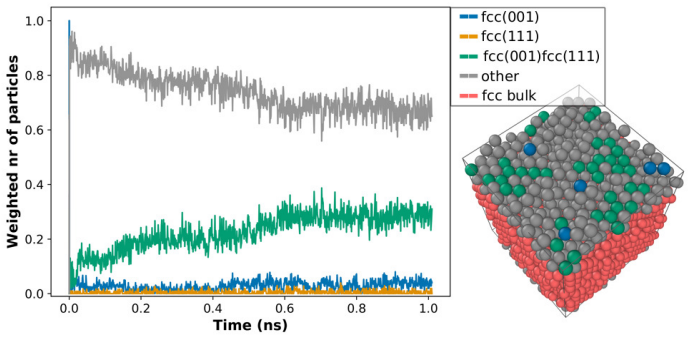

Fig. 3 Crystal structure of the Li surface atoms on a Cu substrate at 300 K. The weighted number of particles is the ratio of particles in a crystal structure over the total amount of surface particles. A snapshot of the simulation cell at 0.8 ns with atoms colour coded in the different crystal structures found using the sa-CNA to the right.

ate transition from the initial fcc(001) surface structure implies that the lattice mismatch between Cu and Li is too large for Li to be stabilized in the fcc surface structure. Interestingly, the surface does not transition into the bcc surface structure, which is included in the other category as it on average constitutes less than 0.1% of the surface atoms. The lack of surface atoms in the bcc structure could arise from the interaction between the uppermost Cu atoms, inhabiting the fcc(001) structure, and the Li surfaces atoms, which guides the Li surface away from the bcc structure and into a vacant and disordered version of the fcc surface structure.

Although the ratio of surface atoms in the unrecognized structure does not directly measure the amount of vacancies in the surface, this structure category also includes atoms in the fcc structure with more than three vacancies. Furthermore, surface atoms in the fcc structure with three or less vacancies constitute more than 8% points of the total amount of atoms in the fcc categories. Together they suggest a high degree of vacancy formation as well as disorder in the Li surface, and supports that vacancies form in the surface as a response to the lattice mismatch between Li and Cu as suggested by the DFT calculations in Tab. 1.

In the MD simulation of the Li surface on the Cu substrate, no diffusion of Li into the Cu substrate is observed. While the diffusion is possible, the energy barrier of diffusion through a Cu thin film was found to be 670 meV, for monovacancy assisted diffusion[35]. The diffusion barrier for inter-layer diffusion is almost three times larger than the SDB of Li (Fig. 1(c)). At 300 K, the corresponding ratio of the diffusion constant of the surface over the inter-layer diffusion, $\frac{D_s}{D_{il}}$, is $19.5 \cdot 10^6$, meaning that the surface diffusion is almost 20 million times faster than the inter-layer diffusion. Consequently, we are not likely to observe inter-layer diffusion on time-scales sufficient to observe surface crystal structure reorganization in the MD simulations, which is the objective of the present work. The diffusion constants are here calculated using

$$D = v\, exp(-\frac{E_b}{k_B T}) \quad (2)$$

where v is the jumping rate, E_b is the diffusion energy barrier, k_B is the Boltzmann constant and T is the temperature. The jumping rate can be estimated through transition state theory, but for the purpose of this work, we assume a similar jumping rate for the surface and inter-layer diffusion.

The Li potential used in this work underestimates the Li melting point by around 70 K, and makes the MD simulation at 300 K is relatively close to the Li melting point found at around 380 K. Since higher degree of disorder is expected for materials close to their melting temperatures, the simulation at 300 K can overestimate the degree of disorder in the Li surface. Therefore, the temperature sensitivity of the surface crystal structure was tested. In Fig. 5(a)-(c) the sa-CNA is performed for MD simulations of the Cu-Li simulation cell at 10 K, 50 K and 150 K. Reducing the temperature to 50 K (Fig. 5(b)) does not affect the amount of disorder in the Li surface significantly. Hence, the vacancies and disorder in the Li surface seen at 300 K is likely to arise from the lattice mismatch between Cu and Li, rather than the temperature.

Interestingly, the fcc(001) surface structure is retained at 10 K (Fig. 5(a)), implying that there is an energy barrier for the transition from the fcc(001) to the disordered structure. Moreover, we find that the fcc(001) surface structure is retained for temperatures up to 150 K when the lattice mismatch is removed, as is the case for a Li surface on a Li substrate. This is shown in Fig. S4(a)-(b)†. In other words, the lattice mismatch on the Cu substrate lowers the barrier to change the Li surface from the close-packed fcc structure to a disordered, vacant and less dense surface structure. Since the Li adatom SDB increases on vacant and less dense Li surfaces on Cu substrates, the Li-Cu lattice mismatch creates a Li surface with high SDBs of the adatoms that might be prone to dendrite formation, rather than facilitating epitaxial growth of fcc Li surface which reduces the SDB and could decrease the amount of dendrites forming on the surface (Fig. 1(b)). Note that even though the surface on the Li substrate is stable in the fcc structure at low temperatures, the Li surface is more disordered at 300 K than it is when supported by the Cu substrate. This is revealed in Fig. 4, showing the surface crystal structure development of the Li surface on a Li substrate at 300 K. Combined with the DFT results, this suggests that the Cu substrate facilitates a higher de-

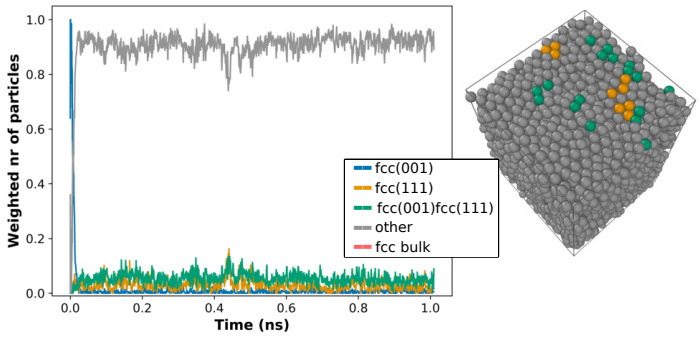

Fig. 4 Crystal structure of the Li surface atoms on a Li substrate at 300 K. The weighted number of particles is the ratio of particles in a crystal structure over the total amount of surface particles. A snapshot of the simulation cell at 0.8 ns with atoms colour coded in the different crystal structures found using the modified sa-CNA to the right.

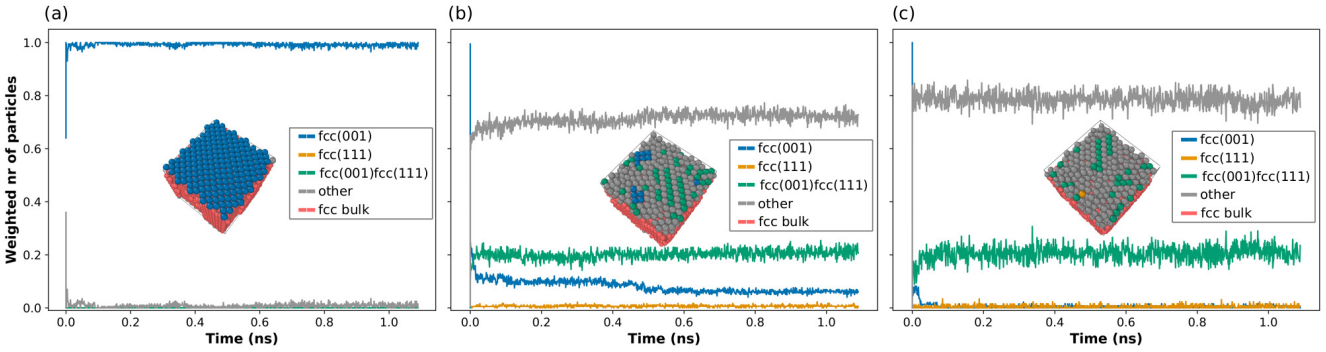

Fig. 5 Crystal structure of the Li surface atoms on a Cu substrate (a) 10 K, (b) 50 K and (c) 150 K. The weighted number of particles is the ratio of particles in a crystal structure over the total amount of surface particles. The insets are snapshots of the respective simulation cells at 0.8 ns, with the atoms colour coded according to the crystal structure found with the sa-CNA.

gree of close-packed Li surface structure, which reduces the SDB and can decrease the amount for dendrite formation, compared to the Li substrate at realistic battery operation temperatures.

Conclusions

In this work, we have studied the impact of the Cu current collector on the surface diffusion barriers (SDB) of Li adatoms using a combination of density functional theory (DFT) and molecular dynamics (MD) simulations. We have developed a surface adaptive Common Neighbour Analysis (sa-CNA) method to analyze the local crystal structure of the Li surface on the Cu substrate which has provided insights into the mechanisms of Li surface diffusion on the Cu substrate.

Using DFT, we found that the Li adatom has high mobility on a Li surface epitaxially grown on the Cu substrate, but due to the Cu-Li lattice mismatch, vacancies are introduced in the surface. The vacancies decrease the density of the surface, which increases the adatom SDB. Furthermore, they increase the importance of the orbital overlap between the Li adatom and the Cu substrate. Owing to the poor s/p-p/d orbital overlap between Li and Cu, the Li adatom SDB increases.

The sa-CNA analyses of the Li surface on the Cu substrate support that vacancies are formed in the surface due to the lattice mismatch between Cu and Li. However, they also indicate that there is an energy barrier for the transition from the close-packed fcc structure to a disordered and vacant structure. This indicates that Li can deposit in the fcc structure with low adatom SDB on substrates that inhabit the fcc structure, provided that the lattice mismatch between the substrate and the Li surface does not introduce vacancies and disorder in the Li surface.

It is challenging to verify the use of the SDB as a sole descriptor for dendrite formation due to the lack of appropriate surface diffusion measurements. Still, this study finds that the combination of low mobility of Li on Cu substrates and the formation on vacancies in the deposited Li layer on the Cu substrate, can make Li prone to dendrite formation. However, we also find that Li might stabilize in a defect-free fcc structure, which can be less prone to dendrite growth, provided that a substrate with the fcc structure and a small lattice mismatch to Li is used.

Conflicts of interest

There are no conflicts to declare.

Acknowledgements

The authors thank Sigma2 for CPU time through the project NN9566k. The Faculty of Natural Sciences at NTNU is acknowledged for financial support.

Notes and references

1 K. Edström, R. Dominko, M. Fichtner, S. Perraud, C. Punckt, P. Asinari, I. E. Castelli, R. Christensen, S. Clark, A. Grimaud, K. Hermansson, A. Heuer, H. Lorrmann, O. M. Løvvik, T. Vegge, W. Wenzel, P. Bayle-Guillemaud, J. Behm, E. Berg, M. Hahlin, S. Hartmann, A. Latz, S. Lyonnard, J. Amici, M. Berecibar, S. Bodoardo, R. Dominko, L. Jabbour, J. Kallo, E.-E. Paillard, O. Raccurt, V. Heiries, N. Guillet, J.-M. Tarascon, D. Van Laethem, E. Ayerbe, R. Diehm, J. Hofmann, O. Miguel, T. Placke, E. Sheridan, P. Barboux, C. Chanson, P. Jacques, M. Meeus, V. Trapp and M. Weil, *Inventing the Sustainable Batteries of the Future*, Battery 2030+ technical report, 2020.

2 P. Albertus, S. Babinec, S. Litzelman and A. Newman, *Nature Energy*, 2018, **3**, 16–21.

3 I. W. Seong, C. H. Hong, B. K. Kim and W. Y. Yoon, *Journal of Power Sources*, 2008, **178**, 769–773.

4 R. Akolkar, *Journal of Power Sources*, 2013, **232**, 23–28.

5 D. R. Ely and R. E. Garcia, *Journal of the Electrochemical Society*, 2013, **160**, A662–A668.

6 X. Xu, Y. Liu, J. Hwang, O. O. Kapitanova, Z. Song, Y. Sun, A. Matic and S. Xiong, *Advanced Energy Materials*, 2020, 2002390.

7 E. Santos and W. Schmickler, *Angewandte Chemie International Edition*, 2021, **60**, 5876–5881.

8 P. Bai, J. Li, F. R. Brushett and M. Z. Bazant, *Energy Environ. Sci.*, 2016, **9**, 3221–3229.

9 K. J. Harry, K. Higa, V. Srinivasan and N. P. Balsara, *Journal of The Electrochemical Society*, 2016, **163**, A2216–A2224.

10 V. Yurkiv, T. Foroozan, A. Ramasubramanian, R. Shahbazian-Yassar and F. Mashayek, *Electrochimica Acta*, 2018, **265**, 609–

619.
11 S. Lv, T. Verhallen, A. Vasileiadis, F. Ooms, Y. Xu, Z. Li, Z. Li and M. Wagemaker, *Nature Communications*, 2018, **9**, 2152.
12 L. Frenck, G. K. Sethi, J. A. Maslyn and N. P. Balsara, *Frontiers in Energy Research*, 2019, **7**, 115.
13 G. Zheng, S. W. Lee, Z. Liang, H.-W. Lee, K. Yan, H. Yao, H. Wang, W. Li, S. Chu and Y. Cui, *Nature Nanotechnology*, 2014, **9**, 618–623.
14 M.-H. Ryou, Y. M. Lee, Y. Lee, M. Winter and P. Bieker, *Advanced Functional Materials*, 2015, **25**, 834–841.
15 X. Wang, W. Zeng, L. Hong, W. Xu, H. Yang, F. Wang, H. Duan, M. Tang and H. Jiang, *Nature Energy*, 2018, **3**, 227–235.
16 X. Chen, X. R. Chen, T. Z. Hou, B. Q. Li, X. B. Cheng, R. Zhang and Q. Zhang, *Science Advances*, 2019, **5**, eaau7728.
17 X. Ma, X. Chen, Y. Bai, X. Shen, R. Zhang and Q. Zhang, *Small*, 2021, 2007142.
18 F. Ding, W. Xu, X. Chen, J. Zhang, Y. Shao, M. H. Engelhard, Y. Zhang, T. A. Blake, G. L. Graff, X. Liu and J. G. Zhang, *Journal of Physical Chemistry C*, 2014, **118**, 4043–4049.
19 Y. Lu, Z. Tu and L. A. Archer, *Nature Materials*, 2014, **13**, 961–969.
20 J. Zheng, M. H. Engelhard, D. Mei, S. Jiao, B. J. Polzin, J. G. Zhang and W. Xu, *Nature Energy*, 2017, **2**, 17012.
21 C. L. Tsai, V. Roddatis, C. V. Chandran, Q. Ma, S. Uhlenbruck, M. Bram, P. Heitjans and O. Guillon, *ACS Applied Materials and Interfaces*, 2016, **8**, 10617–10626.
22 A. C. Kozen, C.-F. Lin, A. J. Pearse, M. A. Schroeder, X. Han, L. Hu, S.-B. Lee, G. W. Rubloff and M. Noked, *ACS Nano*, 2015, **9**, 5884–5892.
23 H. Wang, M. Matsui, H. Kuwata, H. Sonoki, Y. Matsuda, X. Shang, Y. Takeda, O. Yamamoto and N. Imanishi, *Nature Communications*, 2017, **8**, 1–9.
24 E. Cha, M. D. Patel, J. Park, J. Hwang, V. Prasad, K. Cho and W. Choi, *Nature Nanotechnology*, 2018, **13**, 337–344.
25 J. Steiger, G. Richter, M. Wenk, D. Kramer and R. Mönig, *Electrochemistry Communications*, 2015, **50**, 11–14.
26 M. Matsui, *Journal of Power Sources*, 2010, **196**, 7048–7055.
27 M. Jäckle and A. Groß, *The Journal of Chemical Physics*, 2014, **141**, 174710.
28 F. Hao, A. Verma and P. P. Mukherjee, *Energy Storage Materials*, 2019, **20**, 1–6.
29 R. Gomer, *Rep. Prog. Phys*, 1990, **53**, 917–1002.
30 K. J. Harry, D. T. Hallinan, D. Y. Parkinson, A. A. Macdowell and N. P. Balsara, *Nature Materials*, 2013, **13**, 69–73.
31 A. Hagopian, D. Kopač, J.-S. Filhol and A. K. Lautar, *Electrochimica Acta*, 2020, **353**, 136493.
32 I. T. Røe, S. M. Selbach and S. K. Schnell, *Journal of Physical Chemistry Letters*, 2020, **11**, 2891–2895.
33 S. T. Myung, Y. Sasaki, S. Sakurada, Y. K. Sun and H. Yashiro, *Electrochimica Acta*, 2009, **55**, 288–297.
34 P. Zhu, D. Gastol, J. Marshall, R. Sommerville, V. Goodship and E. Kendrick, *Journal of Power Sources*, 2021, **485**, 229321.
35 Z. Xiong, S. Shi, C. Ouyang, M. Lei, L. Hu, Y. Ji, Z. Wang and L. Chen, *Physics Letters, Section A: General, Atomic and Solid State Physics*, 2005, **337**, 247–255.
36 N. Xu, L. Li, Y. He, Y. Lu, L. Li, Y. Lu and Y. Tong, *Journal of Materials Chemistry A*, 2020, **8**, 6229–6237.
37 F. Shen, F. Zhang, Y. Zheng, Z. Fan, Z. Li, Z. Sun, Y. Xuan, B. Zhao, Z. Lin, X. Gui, X. Han, Y. Cheng and C. Niu, *Energy Storage Materials*, 2018, **13**, 323–328.
38 K. Yan, Z. Lu, H.-W. Lee, F. Xiong, P.-C. Hsu, Y. Li, J. Zhao, S. Chu and Y. Cui, *Nature Energy*, 2016, **1**, 16010.
39 L. L. Lu, J. Ge, J. N. Yang, S. M. Chen, H. B. Yao, F. Zhou and S. H. Yu, *Nano Letters*, 2016, **16**, 4431–4437.
40 C. P. Yang, Y. X. Yin, S. F. Zhang, N. W. Li and Y. G. Guo, *Nature Communications*, 2015, **6**, 1–9.
41 G. Kresse and J. Furthmüller, *Computational Materials Science*, 1996, **6**, 15–50.
42 G. Kresse and D. Joubert, *Physical Review B*, 1999, **59**, 1758–1775.
43 H. Jonsson, G. Mills and K. W. Jacobsen, *Classical and Quantum Dynamics in Condensed Phase Simulations - Proceedings of the International School of Physics*, 1998, 385–404.
44 G. Henkelman, B. P. Uberuaga, H. Jónsson and H. Jó, *The Journal of Chemical Physics*, 2000, **113**, 214106.
45 G. Henkelman and H. Jónsson, *Journal of Chemical Physics*, 2000, **113**, 9978.
46 D. Sheppard, P. Xiao, W. Chemelewski, D. D. Johnson and G. Henkelman, *The Journal of Chemical Physics*, 2012, **136**, 74103.
47 P. E. Blöchl, *Physical Review B*, 1994, **50**, 17953.
48 J. P. Perdew, A. Ruzsinszky, G. I. Csonka, O. A. Vydrov, G. E. Scuseria, L. A. Constantin, X. Zhou and K. Burke, *Physical Review Letters*, 2008, **100**, 136406.
49 S. Plimpton, *Journal of Computational Physics*, 1995, **117**, 1–19.
50 M. I. Baskes, *Physical Review B*, 1992, **46**, 2727–2742.
51 W. G. Hoover, *Physical Review A*, 1985, **31**, 1695–1697.
52 H. Okamoto, *Journal of Phase Equilibria and Diffusion*, 2011, **32**, 172–.
53 Y. Zhang and E. J. Maginn, *Citation: The Journal of Chemical Physics*, 2012, **136**, 144116.
54 A. Jain, S. P. Ong, G. Hautier, W. Chen, W. D. Richards, S. Dacek, S. Cholia, D. Gunter, D. Skinner, G. Ceder and K. A. Persson, *APL Materials*, 2013, **1**, 011002.
55 H. P. Davey, *Phys. Rev*, 1925, **25**, 753–761.
56 S. H. Kellington, D. Loveridge and J. M. Titman, *Journal of Physics D: Applied Physics*, 1969, **2**, 1162.
57 D. Sheppard, R. Terrell and G. Henkelman, *Journal of Chemical Physics*, 2008, **128**, 134106–.
58 A. Stukowski, *Modelling and Simulation in Materials Science and Engineering*, 2012, **20**, 045021.
59 A. Stukowski, *Modelling and Simulation in Materials Science and Engineering*, 2010, **18**, 015012.
60 Z. Liu, Y. Qi, Y. X. Lin, L. Chen, P. Lu and L. Q. Chen, *Journal of The Electrochemical Society*, 2016, **163**, A592–A598.

61 M. Jäckle and A. Groß, *Journal of Chemical Physics*, 2019, **151**, 234707.
62 C. Hao, X. Li, Y. Zhang, Y. Xu, Y. Jiang, C. S. Liu, Q. F. Fang, X. Wang and T. Zhang, *Nuclear Instruments and Methods in Physics Research, Section B: Beam Interactions with Materials and Atoms*, 2018, **436**, 51–62.
63 G. J. Ackland, M. Dunuwille, M. Martinez-Canales, I. Loa, R. Zhang, S. Sinogeikin, W. Cai and S. Deemyad, *Science (New York, N.Y.)*, 2017, **356**, 1254–1259.